Modeling the Electromagnetic Scattering Characteristics of Carbon Nanotube Composites Characterized by 3-D Tomographic Transmission Electron Microscopy

As Published: 10.1109/OJAP.2020.2987879

Publisher: Institute of Electrical and Electronics Engineers (IEEE)

Persistent URL: https://hdl.handle.net/1721.1/135388

Version: Final published version: final published article, as it appeared in a journal, conference proceedings, or other formally published context

Received 3 March 2020; revised 6 April 2020; accepted 9 April 2020. Date of publication 14 April 2020; date of current version 7 May 2020.

Digital Object Identifier 10.1109/OJAP.2020.2987879

Modeling the Electromagnetic Scattering Characteristics of Carbon Nanotube Composites Characterized by 3-D Tomographic Transmission Electron Microscopy

AHMED M. HASSAN [1] (Senior Member, IEEE), MD KHADIMUL ISLAM [1] (Graduate Student Member, IEEE), SPENCER ON [1] (Member, IEEE), BHARATH NATARAJAN [2], ITAI Y. STEIN [3], NOA LACHMAN [3], ESTELLE COHEN [3], BRIAN L. WARDLE [3], RENU SHARMA [2], J. ALEXANDER LIDDLE [2], AND EDWARD J. GARBOCZI [4]

[1] Department of Computer Science and Electrical Engineering, University of Missouri–Kansas City, Kansas City, MO 64110, USA

[2] Center for Nanoscale Science and Technology, National Institute of Standards and Technology, Gaithersburg, MD 20899, USA

[3] Department of Aeronautics and Astronautics, Massachusetts Institute of Technology, Cambridge, MA 02139, USA

[4] Material Measurement Laboratory, Applied Chemical and Materials Division, National Institute of Standards and Technology, Boulder, CO 80305, USA

CORRESPONDING AUTHOR: A. M. HASSAN (e-mail: hassanam@umkc.edu)

This work was supported in part by the NIST "Multi-Scale Computational Modeling of Carbon Nanostructure Composites" under Grant 70NANB15H285, and in part by ANSYS, Airbus, Boeing, Embraer, Lockheed Martin, Saab AB, Saertex, and TohoTenax through MIT's Nano-Engineered Composite Aerospace Structures (NECST) Consortium.

ABSTRACT In all prior electromagnetic modeling studies of carbon nanotube (CNT) composites, the exact three-dimensional (3D) shape and spatial distribution of the CNTs in the composite were unknown. Therefore, simplifying assumptions had to be made regarding the CNT distributions. The effect of such assumptions on the electromagnetic response of CNT composites has not been quantified. Recent advances in electron-tomography and image analysis have allowed the generation of 3D maps of multi-walled carbon nanotube (MWCNT) distributions with sub-nanometer resolution. In this work, the electromagnetic responses of experimentally mapped 3D structures of aligned-CNT polymer nanocomposites were calculated using both full-wave electromagnetic solvers and dilute-limit Effective Medium Approximations (EMA). Our results show that the electromagnetic response calculated using the full-wave solver exhibits additional resonances that are absent in the response calculated using the dilute-limit EMA. This difference is due to the strong electromagnetic coupling between adjacent MWCNTs, within five CNT radii, of each other. Using the mapped 3D MWCNTs, we also studied the anisotropy in the electromagnetic response of the composites and showed that it increases with the MWCNT volume fraction. The full-wave analysis presented in this work provides a more accurate understanding of the electromagnetic reflection and anisotropy of CNT composites.

INDEX TERMS Nanocomposites, carbon nanotubes, electromagnetic modeling nanophotonics, nanowires, electromagnetic shielding, reflection coefficient, nonhomogeneous media, computational electromagnetics.

I. INTRODUCTION

CARBON nanotubes (CNTs) are considered the additive of choice in a wide range of applications due to their exceptional electrical, mechanical, chemical, and biological properties. In many cases, CNTs are added to a polymer matrix to create a composite with enhanced properties that cannot be achieved by the components on their own. One of the recent applications of CNT composites is as advanced electromagnetic shielding films [1]. In shielding applications, the goal is to create a lightweight

composite with considerable shielding in the microwave range. Here, CNTs are added to a low-density polymer, which is transparent in its undoped state to microwave radiation, to create a light and tunable composite with high shielding effectiveness [1], [2]. CNT composites have also recently been proposed for thermotherapy [3]. In this case, the goal is to develop a composite that is stretchable, stable, and can still achieve fast electrical heating [3]. Kim *et al.* recently demonstrated a multi-walled carbon nanotube (MWCNT) silicon emulsion composite with a fast-heating behavior of up to 4.8 °C/s that can be maintained over 100 cycles [3]. The thermal properties of the composites can be tuned by varying the density of the CNTs [4]. For example, Marconnet *et al.* reported a greater than linear increase in the overall thermal conductivity of the composite with a linear increase in CNT volume fraction [4]. Several other studies have recently shown that MWCNT composites can be used as multifunctional scaffolds for the tissue engineering of cardiac muscle cells called cardiomyocytes [5]. In addition to improving the mechanical properties and the structural integrity of the scaffold, the conductivity of the MWCNTs improved the electrical stimulation and conductivity of the grown cardiomyocytes [5]. One of the main applications of CNT composites is as sensors in a wide variety of chemical and biological applications [6]. For example, Liu *et al.* reported sensors fabricated from CNT composites for detecting acid penetration. The response time of the sensor was found to be dependent on the concentration of the CNT additives added to the composite [6]. The previous examples represent a small sample of the CNT composite applications currently being pursued. Additional examples can be found in several reviews such as in [7], [8].

In all of these applications, the desired functionality is highly dependent on the properties of the CNT additives and their exact distribution or dispersion in the composite [1], [2], [9]. Hence, an accurate non-contact method for the evaluation of CNT properties and distribution is important to advance all of these applications. Recently, the use of electromagnetic waves in the microwave, millimeter, and THz range have been evaluated, experimentally and computationally, as techniques for the nondestructive evaluation (NDE) of CNT composites [10]–[16]. However, for these NDE techniques to be successful, the correlation between CNT properties/distributions and the electromagnetic response needs to be accurately delineated. Different methods have been investigated to calculate the electromagnetic response of CNT composites with a particular CNT distribution [17]. In these studies, the exact three-dimensional (3D) distribution of the CNTs in the composite was unknown. Therefore, the CNTs were assumed to be all perfectly aligned [18]–[20] or to be randomly oriented [17].

Moreover, the relationship between the overall electrical properties of the composites and the conductivity of a single CNT were assumed to obey the dilute limit effective medium approximations (EMA) such as the Waterman-Truell [18]–[20] or the Maxwell Garnett formulations [21]. These assumptions were used in the retrieval of the conductivity of a single CNT from the experimentally measured electromagnetic response of a composite containing thousands or millions of CNTs [17]–[21]. However, to the best of our knowledge, the accuracy of these assumptions has not been quantified. To this end, the primary goal of this paper is to investigate the accuracy of the electromagnetic response calculated using the dilute limit EMA of a simplified CNT distribution by comparing against the full-wave electromagnetic response of a realistic CNT distribution.

This comparison has thus far been difficult to carry out since the exact 3D CNT geometries and distributions in a composite have been inaccessible. CNT composites are typically characterized using 2D scanning electron microscopy (SEM) and/or transmission electron microscopy (TEM) images, which only provide 2D projections or cross-sections of the complex 3D CNT distributions [22]. However, in a seminal study by Natarajan *et al.*, high-quality 3D reconstructions of the morphology and distribution of MWCNTs in a composite, with nanoscale resolution, were achieved using electron tomography [23]. This tomography study provided extensive information regarding the shape, alignment, and level of waviness of each CNT, and quantified the evolution of these parameters with increasing MWCNT volume fraction [23].

In this work, we use these innovative 3D maps as numerical testbeds for calculating the electromagnetic response of CNT composites. That is, we assign the same conductivity value to all the MWCNTs in the reconstructed composite, simulate the composite using multiple full-wave solvers, and then investigate how much the calculated response agrees with the commonly employed EMA response. This comparison will allow us to predict, with higher accuracy, the electromagnetic response of CNT composites. Moreover, the EMA is currently employed to interpret experimental measurements and, therefore, by quantifying its limitations we can more accurately interpret experimental measurements on CNT composites.

This paper is organized as follows. Section II describes the process of fabricating composites with highly aligned MWCNTs and the steps used for the 3D electron tomographic imaging of the composite. Section III describes the different conductivity models used for each CNT. In Section IV, the calculation of the electromagnetic response of MWCNT composites using full-wave techniques and using the EMA is presented and discussed. Computational results are presented in Section V and Conclusions and future work are discussed in Section VI.

II. FABRICATION AND 3D ELECTRON TOMOGRAPHY OF MWCNT COMPOSITES

Different applications require CNTs with different sizes, shapes, distributions, and volume fractions inside an embedding matrix. Volume fraction is a dimensionless quantity, which is calculated by dividing the total volume of the

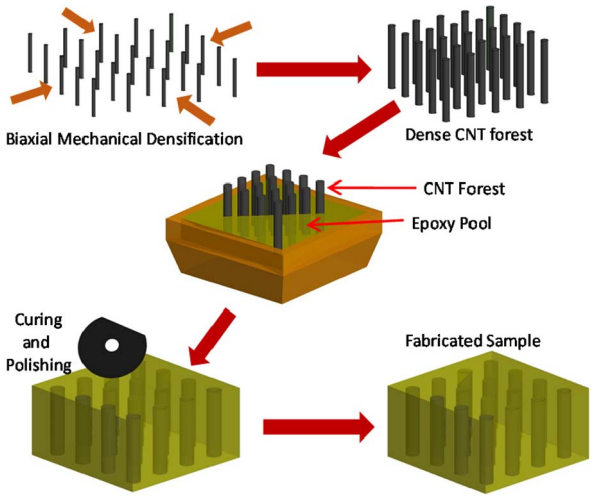

FIGURE 1. Fabrication steps of the composites studied in this paper showing how the density of the MWCNTs was increased via biaxial mechanical forces.

CNTs by the overall volume of the composite. That is, volume fraction is a measure of the CNT concentration in the composite. Numerous techniques have been developed to fabricate CNT composites while controlling the aforementioned parameters [24]–[28]. In many cases, highly aligned CNTs are desired to improve the overall mechanical and electrical properties of the composite [28]–[30]. The 3D MWCNT composites studied in this work were fabricated using a process similar to the one summarized in Fig. 1 as detailed in [24]. Briefly, chemical vapor deposition (CVD) was used to grow forests of millimeter-long highly aligned MWCNTs on a silicon substrate. The MWCNTs have an average outer radius of approximately 3.83 ± 0.44 nm and an inner radius of 2.5 nm. In all subsequent analysis, we will assume that the MWCNTs have an outer radius of 3.86 nm and an inner radius of 2.5 nm, which will yield approximately 5 walls per tube assuming that the inter-wall spacing is 0.34 nm, the interlayer spacing in graphite [31]. The MWCNT forest had an approximate volume fraction of 0.5 % [24]. To increase the volume fraction, the MWCNT forest was detached from the silicon substrate and densification was performed by applying mechanical compression from the two directions perpendicular to the axis of the MWCNTs, to bring the MWCNTs closer together as shown in Fig. 1 [24]. The advantage of this fabrication technique is that by tuning the mechanical compression, a wide range of MWCNT volume fractions could be achieved [24]. The densified MWCNT forest was then infiltrated with a liquid aerospace-grade epoxy, which was absorbed through the voids between the MWCNTs via capillary effects. The mixture was then cured and polished to finish the preparation of the MWCNT-epoxy composite.

Following their fabrication, four composites with different MWCNT volume fractions were imaged using 3D quantitative electron tomography [32]. The MWCNT samples were sliced using focused ion beam milling into 200 nm thick layers to facilitate TEM imaging. Gold nanoparticles, 5 nm in radius, were added to the MWCNT composite to act as image alignment markers. Multiple images were collected by tilting the sample at multiple angles. However, because of limitations in the hardware setup, the sample could not be rotated a full 360° to get images from every possible angle and views were lacking over a total of 120°, from $-60°$ to $+60°$. Inspite of this limited view, these images were stacked to create a detailed 3D map of the MWCNTs in the composite using the simultaneous iterative reconstruction technique (SIRT) and the gold nanoparticles for alignment [23]. The images were segmented to identify the coordinates of the MWCNTs using an automated technique developed in [23]. Figure 2(a) shows one example of the experimentally reconstructed MWCNT map obtained by imaging an 800 nm $\times$ 800 nm $\times$ 200 nm volume of the fabricated composite. The variations in the radii of the MWCNTs were much smaller than the variations in their lengths. Therefore, all MWCNTs were assumed to have the same previously mentioned values for their radii. They are shown using a set of different colors in Fig. 2(a) for visual clarity and to facilitate the identification of different MWCNTs, for a total of 232 MWCNTs. The composite in Fig. 2 had a total MWCNT volume fraction of 0.5% which was calculated by adding up the total volume of the 232 reconstructed MWCNTs and dividing by the volume of the unit cell, 800 nm $\times$ 800 nm $\times$ 200 nm $= 1.28 \times 10^8$ nm^3. Other ways to calculate the MWCNT volume fraction in a composite is the weight method [23]. In the weight method, the mass of the composite after the MWCNTs are added is compared to the mass of an empty epoxy substrate with a similar size. The difference between the two masses will be the mass of the MWCNTs only, which when divided by the mass of the composite will provide the weight fraction of the MWCNTs. The knowledge of the densities of the MWCNTs and that of epoxy can be then used to convert this weight fraction into volume fraction [23]. However, the weight method contains many uncertainties and calculating the volume fraction from the reconstructed 3D distribution of the MWCNTs, similar to Fig. 2a, provides a more accurate estimate of the true volume fraction [23].

The length distribution of these tubes is plotted in Fig. 2(b), which shows that most of the MWCNTs have contour lengths that are less than 100 nm and that few MWCNTs are longer than 200 nm. The MWCNTs in the fabricated sample were significantly longer than the ones shown in Fig. 2. However, 3D electron tomography is limited to imaging small domains similar to the region studied in Fig. 2 [23]. Therefore, some of the MWCNTs seen in the reconstructions in Fig. 2 might be sections of longer MWCNTs. However, the main advantage of the 3D reconstructed maps is to show the true shape of the MWCNTs and the fact that they are not all perfectly straight and aligned. Moreover, the 3D reconstructed maps quantify how close the MWCNTs are to each other and how this closeness varies with the MWCNT volume fraction. The waviness of the MWCNTs and their closeness to each other has a significant

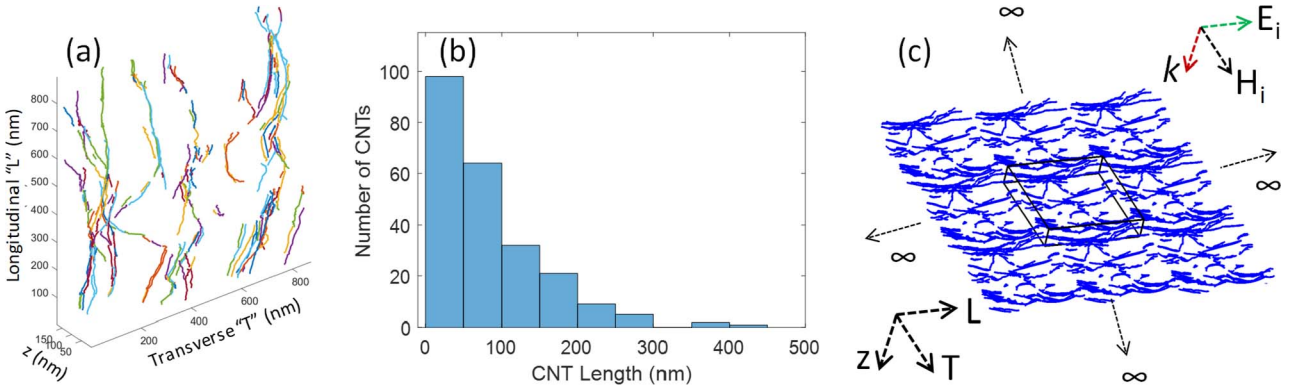

FIGURE 2. Multi-wall carbon nanotube (MWCNT) morphological information: (a) Experimentally reconstructed map showing the line-contours of 232 MWCNTs in a composite. The MWCNTs occupy 0.5 % of the total volume of the composite and are shown in a set of different colors to facilitate identifying close but separate MWCNTs, (b) Histogram showing the MWCNT lengths distribution, (c) a sketch showing the effective MWCNT composite simulated after enforcing double periodic boundary conditions. The MWCNTs enclosed in the box in the center show the unit cell in Fig. 2a and the arrows E_i, H_i, and k indicate the directions of the electric field, magnetic field, and incident wave, respectively.

impact on the electromagnetic response as will be discussed in the following sections. Also, many of the reconstructed MWCNTs, started and ended within the imaging domain of the electron tomography, away from the boundaries, indicating that they represented a complete MWCNT and not just a section. Therefore, we opted for modeling the reconstructed distribution in Fig. 2 since it accurately represents the waviness, alignment, and the spacing between the MWCNTs. However, in Section V, we will also simulate longer MWCNTs, artificially generated to qualitatively resemble the shapes in Fig. 2, in order to have insight on the response of MWCNTs comparable in length to the originally manufactured composite.

The MWCNTs in Fig. 2(a) are highly aligned with the Longitudinal "*L*" axis and are actually straighter than most commercial and research-grade MWCNT composites [24]. However, it is clear from the figure that none of the MWCNTs are perfectly straight and that some of them are misaligned. Moreover, the MWCNTs cannot be thought of as perfectly randomly oriented since there is a general alignment with the "*L*" axis. In other words, these MWCNTs exhibit complex geometries and distributions that differ from the simple assumptions that are typically used in describing the distribution of MWCNTs in composites. Our goal is to quantify the differences between the electromagnetic response calculated using the exact MWCNT geometries and distributions in Fig. 2(a) versus that calculated under the assumption that all the MWCNTs are perfectly aligned. The frequency range of interest is from microwaves to the upper Terahertz (THz) region (1 GHz to 30 THz), or wavelengths varying from the centimeter to the micrometer range.

Typically the incident waveform can be focused into a spotsize that is proportional to the wavelength. Therefore, the imaged volume should ideally have dimensions that are comparable to the wavelength of the incident electromagnetic radiations. However, the 3D electron tomography of such a huge volume with sub-nanometer resolution is unrealistic [23]. Nevertheless, we performed reconstruction of regions with similar volumes to that shown in Fig. 2(a) from different parts of the composite and quantitative assessments demonstrated that the map shown in Fig 2(a) is a good representation of the MWCNT distribution in the rest of the composite [23]. Therefore, periodic boundary conditions are enforced on the reconstructed MWCNT map to extend its spatial content to infinity, emulating MWCNT laminates whose lateral dimensions are significantly larger than their thickness. A representation of this infinitely periodic structure is shown in Fig. 2(c).

III. COMPUTATIONAL MODELING

A. CONDUCTIVITY MODELS OF MWCNT

For simplicity, we assume that all MWCNTs in the composite have the same conductivity, since the main goal of this work is to investigate how the shape and distribution of the MWCNTs affect composite electromagnetic properties. It is challenging to experimentally measure the conductivity of individual MWCNTs, especially after the MWCNTs are mixed with epoxy to form the composite. Therefore, we will investigate multiple values for the MWCNT conductivity to cover the range of values reported in various theoretical models (see [31], [32] for example). In a practical sample, different MWCNTs might have different conductivities. However, as a starting point, we will assume that within one sample all MWCNTs have the same conductivity similar to the previously reported analyses where the conductivity of all CNTs in the composites were assumed to be the same [21].

In general, most fabricated CNT samples contain both metallic and semiconducting tubes. Recently several studies have reported different techniques to enforce the selection of either metallic walls or semiconducting walls during fabrication [33]. Etching using oxygen or water vapor is typically employed to remove metallic CNTs from a fabricated sample due to the higher reactivity of the metallic CNTs [33]. On the other hand, the removal of semiconducting CNTs from a sample is typically achieved by

optimizing the annealing process of the catalysts used to grow the CNTs [33]. However, in this work, no conditions were enforced in the fabrication process to favor metallic or semiconducting CNTs.

Dividing the difference between the outer (3.86 nm) and internal (2.5 nm) radii of the MWCNT with graphite's interlayer separation of 0.34 nm gives 5 walls per each MWCNT. If we assume that the inner wall has a radius of exactly 2.5 nm, then the walls of the MWCNTs will have the following radii: {2.5 nm, 2.84 nm, 3.18 nm, 3.52 nm, 3.86 nm}. Each radius corresponds to a different wall with a different structure. The structure of a CNT wall is typically defined by its chirality, which is defined by two integer indices, (n, m) with $n \geq m$ by convention [34]. The chirality can be a strong determinant of the wall's electrical and mechanical properties [34]. However, the relationship between the radius of a wall and its chirality is not unique. That is, many different CNT chiralities can yield exactly the same radius [34]. In this paper, we reconstructed the radii of the walls constituting the MWCNT with high accuracy but the exact chirality of each wall was ambiguous. Therefore, Table 1 lists all possible chiralities that provide the same radius as the walls constituting the MWCNT. That is, for every one of the five walls, we searched for all possible chiralities within $\pm$ 0.1% of its radius and listed these chiralities in Table 1.

Based on the chirality, each of the MWCNT walls can be metallic or semiconducting. CNT walls can be metallic or semiconducting based on the chirality values (n, m) with $n \geq m$ by convention. If the difference $(n - m)$ is divisible by three then the wall is metallic; otherwise, it is semiconducting [34]. The chiralities in Table 1 are divided into semiconducting and metallic walls based on this condition. The significance of Table 1 is to show that there is at least one possible chirality to make each wall metallic or semiconducting.

In an uncontrolled growth, there is a probability that all 5 MWCNTs walls are metallic or all of them are semiconducting. However, on average one-third of the walls are usually metallic since statistically only chiralities with $(n-m)$ divisible by three are metallic. Therefore, on average, approximately two walls out of the five in Table 1 will be metallic and three will be semiconducting [32]. However, to cover all possible MWCNT conductivities, we are going to study two configurations. In the first configuration, each MWCNT will have 5 metallic walls as shown in Fig. 3a. In the second configuration, each MWCNT will have only two metallic walls, primarily wall 2 and wall 5, and the three other walls will be semiconducting, Fig. 3b-3d. These two cases are similar to the two cases considered in the study of MWCNT as wave guides and antennas reported in [32].

Semiconducting walls have significantly lower conductivities than the metallic walls and, therefore, their contribution can be neglected in the microwave and terahertz range [20], [35], [36]. As for the metallic walls, different chiralities with the same radius have approximately the same

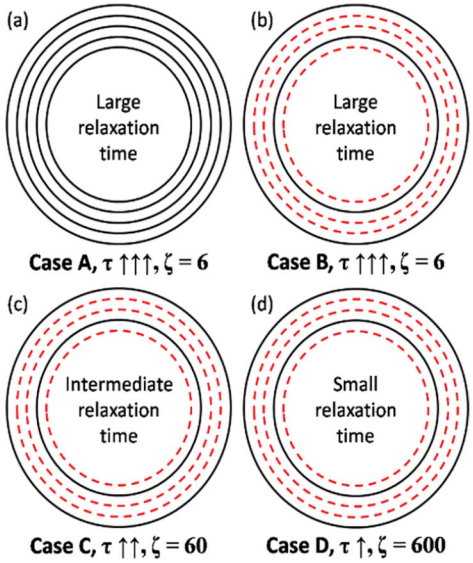

FIGURE 3. A sketch showing the four MWCNT conductivities studied in this work: (a) five metallic walls in solid black with large relaxation time, (b) two metallic walls, shown in solid black, and three semiconducting walls, shown in dashed red, with large relaxation time, (c) two metallic walls and three semiconducting walls with an intermediate relaxation time, and (d) two metallic walls and three semiconducting walls with a small relaxation time.

conductivity, as discussed in [34]–[36]. That is, chiralities (56, 26) and (67, 10) have the same radius of 2.84 nm and they will have the same conductivity. Therefore, determining which walls are metallic and the knowledge of the radius of each wall is sufficient to determine the conductivity of each wall and to define the overall conductivity of the MWCNT, as will be defined in the following semi-classical analysis.

In this work, we will only focus on the frequency range between 1 GHz to 30 THz, where the inter-band conductivity of the CNT walls can be typically neglected [35], [36]. Using a semi-classical approach, the intra-band surface conductivity of the w^{th} wall in the MWCNT, σ_{w}, can be expressed as [35], [36]:

$$\sigma_w = \frac{je^2}{2\pi^2 R_w \hbar^2 (\omega - j/\tau)} \times \sum_{s=1}^{n} \int_{-R_{cnt}}^{R_{cnt}} \frac{\partial \varepsilon_c(p_z, s)}{\partial p_z} \frac{\partial \rho^{eq}(p_z, s)}{\partial p_z} dp_z \qquad (1)$$

where j is the square root of -1, e is the charge of an electron, R_w is the radius of the w^{th} wall which can be calculated in terms of the wall's chirality (n, m) as $R_w = ((b\sqrt{3})/(2\pi))\sqrt{(n^2+nm+m^2)}$, $\hbar$ is the reduced Planck's constant, ω is the radial frequency, τ is the electron relaxation time, n is the CNT chirality index (n, m), $\varepsilon_c(p_z, s)$ is the energy dispersion relationship of the conduction band, $\varepsilon_v(p_z, s)$ is the energy dispersion relationship of the valence band, p_z is the momentum component along the axis of the carbon nanotube, and $\rho^{eq}(p_z, s) = F(\varepsilon_c(p_z, s)) - F(\varepsilon_v(p_z, s))$, where $F(\varepsilon_v(p_z, s))$ represents the Fermi distribution. For chiralities with small n and m values, the intra-band surface conductivity of a single CNT wall can be approximated

TABLE 1. Chiralities that match the MWCNT radii experimentally measured from the composite.

Wall	Radius	Semiconducting Chiralities (n, m)	Metallic Chiralities (n, m)
1	2.5 nm	(50,22), (55,15)	(57,12)
2	2.84 nm	(51,32), (59,22), (71,3), (72,1)	(56,26), (67,10)
3	3.18 nm	(62,30), (68,22), (72,16), (74,13)	(57,36), (65,26), (70,19), (77,8), (78,6)
4	3.52 nm	(63,40), (68,34), (71,30), (82,14), (85,9)	(62,41), (74,26)
5	3.86 nm	(68,45), (69,44), (77,34), (85,23), (87,20), (92,12), (95,7), (96,5), (97,3), (98,1)	(74,38), (83,26), (89,17)

using the Drude-like expression [35], [36]:

$$\sigma_w = j\frac{3b\gamma_0 e^2}{\pi^2 R_w \hbar^2(\omega - j/\tau)} \tag{2}$$

where b is the carbon interatomic distance ($b = 0.142$ nm) and $\gamma_0 = 2.7$ eV. The relaxation time τ can be expressed as [31], [37]:

$$\tau = \nu^{-1} = \frac{R_w}{\zeta Te} \tag{3}$$

where ν is the relaxation frequency, Te is the temperature, and ζ is a fitting parameter to be determined typically experimentally [37]. Since τ is dependent on the radius of the wall as shown in (3), different walls in an MWCNT will have different relaxation times due to variations in their radii. The Drude model approximation in (2) yields accurate conductivity results, for the chiralities used in this work as shown in Table 1, within 0.5 % of the values calculated by the model in (1). The τ values reported in the literature typically vary in the 10^{-14}s $-$ 10^{-12} s range [18]–[20] and [37]–[38]. To cover the variations in the relaxation time, τ, reported in the literature, three values of ζ were investigated: 6 m/Ks, 60 m/Ks, and 600 m/Ks for the metallic wall configurations in Fig. 3 [37], [38]. Table 2 shows the ζ values and the corresponding relaxation time for the 5^{th} wall, τ_5. The other 4 walls will have a lower relaxation time due to their smaller radius as indicated by (3). Table 2 shows that the higher the value of ζ, the lower the relaxation time τ, and the lower the DC conductivity of the CNT wall. Table 2 also shows that our choice of the ζ parameter yields τ values in the 10^{-14}s $-$ 10^{-12} s range similar to the values commonly reported in the literature [18]–[20] and [37]–[38].

In summary, the conductivity of an individual MWCNT will vary according to the number of metallic walls and the value of the relaxation time assigned to these metallic walls. In total, four different conductivity permutations were used in the computational experiments conducted in this work. These four cases are summarized in Table 2 and Fig. 3.

The overall effective bulk conductivity of an MWCNT, σ_{3D}, can be estimated by adding in parallel the individual surface conductivities of its walls, σ_w, as follows [31]:

TABLE 2. Description of MWCNT conductivity models used (see Fig. 3).

Case	# of Metallic/# of Semi-Conducting Walls	Relaxation-Time Param. for metallic walls ζ (m/Ks)	τ_5 (10^{-12} s)
A	5/0	6	2.2
B	2/3	6	2.2
C	2/3	60	0.22
D	2/3	600	0.022

$$\sigma_{3D} = \frac{2}{(R_5)^2}\sum_{w=1}^{5} R_w \sigma_w \tag{4}$$

where R_5 is the radius of the outer wall of the MWCNT, 3.86 nm. Figure 4(a) and Figure 4(b) show the real and imaginary parts of σ_{3D}, respectively, for the four cases described in Table 2. The corresponding complex relative dielectric permittivity, ε_r, of the MWCNT can be expressed as:

$$\varepsilon_r = 1 - j\frac{\sigma_{3D}}{\omega\epsilon_0} \tag{5}$$

Note that since the conductivity σ_{3D} is complex, the overall real part of ε_r is nonunity. Figure 4(c) and Figure 4(d) show the real and imaginary parts of σ_{3D}, respectively, for the four cases described in Table 2. Without loss of generality, the MWCNTs will be assumed to be embedded in air forming a network or a thin film. That is, the relative permittivity of the embedding medium is unity, $\varepsilon_h = 1$. In the future, we plan to extend our study to MWCNTs embedded in polymer laminates with different permittivities and dimensions.

B. ELECTROMAGNETIC MODELING OF MWCNT COMPOSITES

Full-Wave Response: Full-wave electromagnetic analysis provides the most accurate but the most computationally complex approach for calculating the electromagnetic response of the MWCNT composites. To validate our results, we used two independent commercial full-wave electromagnetic solvers to calculate the electromagnetic response of the MWCNT composites: (*i*) FEKO, a Method of

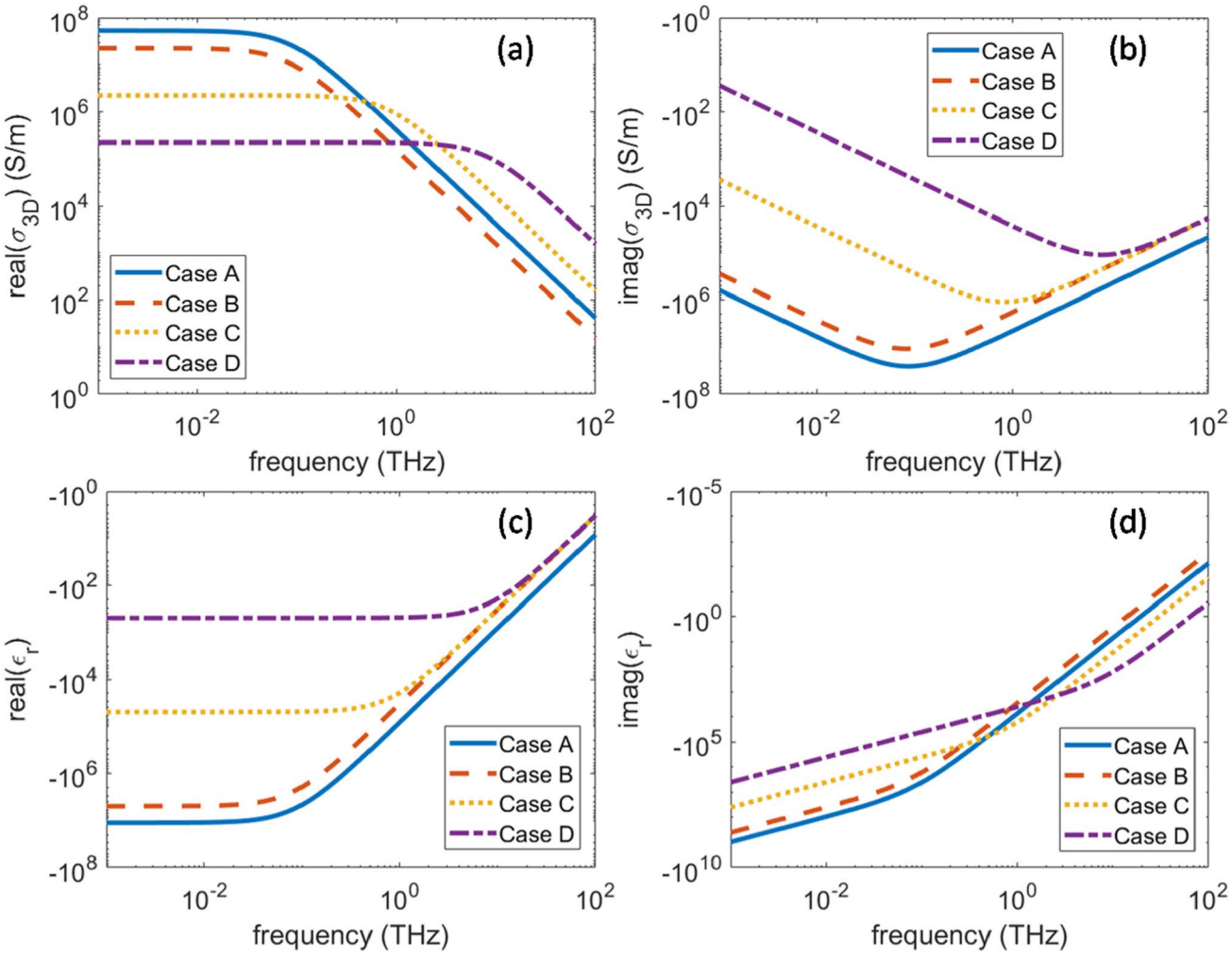

FIGURE 4. Effective bulk conductivity of a single MWCNT for the different cases considered in Table 2 and Fig. 3: (a) Real part of the overall effective bulk conductivity, σ3D, of a MWCNT, (b) imaginary part of σ3D of a MWCNT, (c) Real part of the overall complex relative dielectric permittivity of the MWCNT, and (d) imaginary part of the overall complex relative dielectric permittivity of the MWCNT.

Moments (MOM) based solver [39] and (*ii*) CST Microwave Studio (MWS), a FEM based solver [40]. We used both FEKO and CST MWS to calculate the electromagnetic response of the composite shown in Fig. 2. Due to the complexity and the large number of MWCNTs in the composite, some of the computational simulations required several hours and even several days to complete. Therefore, in our validation example, we only included the 10 longest MWCNTs in the sample in Fig. 2 and we simulated the ensuing composite using both FEKO and CST MWS. However, the MWCNTs were simulated with their exact reconstructed shapes and locations. The simulated geometry is shown in Fig. 5(a) alongside with the incident electric field which is in the vertical direction as shown by the green arrow. The incoming wave is propagating in the direction perpendicular to the plane shown in Fig. 5a. Periodic boundary conditions were enforced in the "*L*" and "*T*" directions to create a composite composed of an infinite array of the unit cell shown in Fig. 5(a). The size of the unit cell in "*L*" and "*T*" is 882 nm $\times$ 910 nm. In the z-direction, the direction perpendicular to the infinite plane in Fig. 1c, the MWCNTs were distributed over a distance of 185 nm giving the composite an effective thickness of 185 nm. That is, the highest MWCNT pixel in the composite was placed at a height z $=$ 0 nm and the deepest MWCNT pixel was located at z $=-185$ nm. The conductivity model described as Case A (all walls metallic and large relaxations time) in Table 2 was assigned to each MWCNT.

The array was excited using a plane wave propagating normal to the array, in the z-direction, and the polarization was parallel to the "*L*" axis, as indicated in Fig. 5(a). The magnitude and phase of the reflection from the composite were then calculated at $z = 0$ nm using both FEKO and CST MWS and plotted in Fig 5(b) and Fig. 5(c), respectively. Excellent agreement between the magnitude and phase of the reflection coefficient is achieved between both independent solvers, FEKO and CST MWS, validating our results. Similar agreements were achieved for different MWCNT

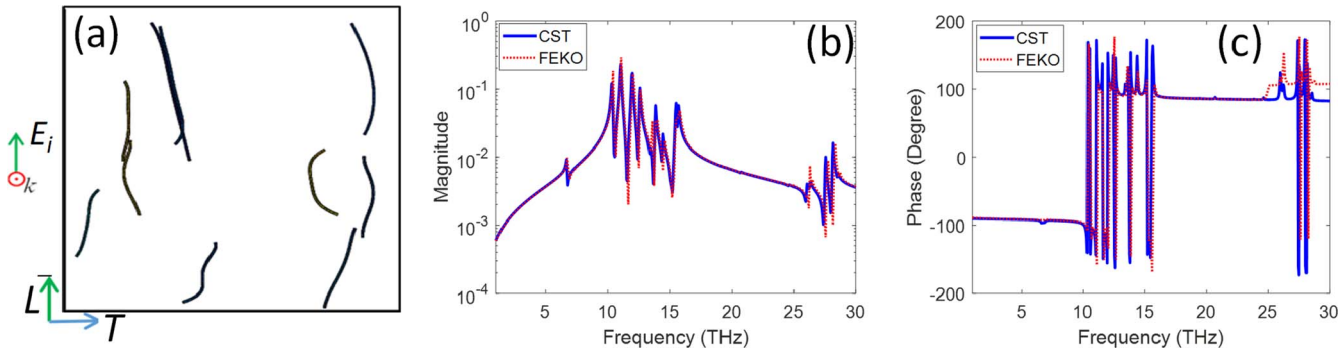

FIGURE 5. Validation results: (a) Unit cell showing only the longest 10 MWCNTs simulated using both FEKO and CST MWS. The incident electric field is in the vertical direction as shown by the green arrow, (b) Magnitude of the reflection coefficient, and (c) Phase of the reflection coefficient as calculated from the composite whose unit cell is shown in Fig. 5a.

distributions and different conductivity models. Therefore, in the following sections, only the CST MWS results will be presented.

Dilute Limit Effective Medium Approximation: The dilute limit EMA does not require the knowledge of the exact distribution of the inclusions in the composite but only their volume fraction and orientation. Therefore, in most reported studies, the effective dielectric properties of a composite were estimated using the dilute limit EMA, since the exact shapes and distributions of the composite were inaccessible. The first step in most EMAs typically involves calculating the polarizability of each MWCNT. The polarizability of an arbitrary shaped MWCNT can be evaluated using the MOM for Arbitrary Thin Wire (ATW) approach [12], [13], [41] as:

$$\boldsymbol{\alpha} = -\frac{j}{\omega\varepsilon_0}\int_0^L \mathbf{J}(\ell)d\ell \tag{6}$$

where ε_0 is the permittivity of free space, J(l) is the MWCNT axial current due to an incident excitation, and L is the length of the MWCNT. Equation (6) summarizes the nine components of the polarizability tensor, of which six are independent. For example, to calculate the α_{xy} component, the incident electric field is set in the x-direction and the y-component of the axial current J(l) is selected in the integration in (6) [12]. The MWCNTs in the samples considered in this work have a general alignment with the *"L"* axis as shown in Fig. 2. Therefore, for comparison with the full-wave simulation, the electric field polarization was parallel to the *"L"* axis and the parallel polarization of the reflected wave was selected. Several studies have shown that for straight CNTs, the polarizability in (6) can be approximated with high accuracy using the polarizability of a prolate ellipsoid as follows [18]:

$$\alpha = \frac{4\pi a_1 a_2 a_3}{3}\frac{\varepsilon_r(\omega)-\varepsilon_h}{\varepsilon_h + D(\varepsilon_r(\omega)-\varepsilon_h)} \tag{7}$$

where α is the polarizability component parallel to the length of the CNT. The parameters a_1, a_2, and a_3 are the radii of the ellipsoid and for the case of MWCNTs they can be approximated as $a_1 = a_2 = R_5$ and $a_3 = L/2$. The parameter D is the depolarization factor that can be calculated along the major axis of the prolate ellipsoid as [18]:

$$D = \frac{x}{2(x^2-1)}\left(\frac{1}{\sqrt{x^2-1}}ln\left(\frac{x+\sqrt{x^2+1}}{x-\sqrt{x^2-1}}\right) - \frac{2}{x}\right) \tag{8a}$$

$$x = \frac{L}{2R_5} \tag{8b}$$

The parameter ε_h represents the relative dielectric permittivity of the surrounding medium, assumed to be air in this work ($\varepsilon_h = 1$), and $\varepsilon_r(\omega)$ is the dielectric constant of the MWCNT, which can be calculated using (5). The polarizability approximation in (7-8) provides a good approximation for the polarizability of straight MWCNTs [18]. The MWCNTs in the samples considered herein are fabricated to be highly aligned and, therefore, they can be considered to be "practically" straight. However, several of the MWCNTs show relatively high curvature, as shown in Fig. 2. Therefore, by employing the approximation in (7-8) we will test the validity of the assumption that MWCNTs can be considered straight in practical composites with highly aligned MWCNTs.

Using either (6) or (7) for the polarizability α, the effective relative permittivity of the composite can be estimated using the dilute limit EMA. In this work, the Waterman-Truell Formula for EMA is used to calculate the effective dielectric permittivity of the composite as follows:

$$\varepsilon_{eff} = \varepsilon_h + \sum_{i=1}^{N}\alpha(\omega, L_i)\phi(L_i) \tag{9}$$

where L_i is the length of MWCNT i, N is the number of MWCNTs in the unit cell ($N = 232$ in the sample in Fig. 2), and $\phi(L_i)$ is the volume fraction of MWCNT i calculated by dividing the volume of MWCNT i with the volume of the unit cell. Using ε_{eff} and the presumed thickness of the sample, the overall reflection from the composite, R, due to a plane wave at normal incidence, can be calculated using the Nicholson and Ross equations as follows:

$$R = \frac{(1-T^2)\Gamma}{(1-T^2\Gamma^2)} \tag{10a}$$

$$T = exp\left(-j\omega\sqrt{\mu_0\varepsilon_0\varepsilon_{eff}}d\right) \tag{10b}$$

$$\Gamma = \frac{1 - \sqrt{\varepsilon_{eff}}}{1 + \sqrt{\varepsilon_{eff}}} \tag{10c}$$

where T is the transmission coefficient at the top interface of the effective composite, Γ is the reflection coefficient at the air/composite interface, d is the thickness of the composite, and μ_0 is the magnetic permeability of free space. Even though in our simulations the MWCNTs were embedded in free space, an effective thickness of the composite was designated as the difference between the height of the highest segment of the top MWCNT and the height of the lowest segment of the bottom MWCNT.

The main limitation of the dilute limit EMA in (9) is that it ignores the interactions between the CNTs. This limitation is typically justified by the low volume fraction of the CNTs inside the composite, which typically leads to large separations between the individual CNTs. However, as can be seen in Fig. 2, some CNTs are quite close, and therefore will exhibit strong interactions, even though the total CNT volume fraction is below 0.5 %. The second approximation in (7)-(9) is the assumption that the MWCNTs are straight so that their polarizabilities can be approximated by that of a prolate ellipsoid. Each of the above two approximations are frequently employed in the literature. The effect of these approximations on the effective properties of the composite will be quantified by comparing with the response calculated using the full-wave simulations.

IV. RESULTS AND DISCUSSION

The main goal of this section is to contrast the electromagnetic response calculated using the dilute limit effective medium approximation with that calculated using the full-wave solvers for the reconstructed 3D MWCNT distributions. We also study the electromagnetic response of simple MWCNT distributions to explain the results achieved from the reconstructed MWCNT distributions. Finally, we use the reconstructed 3D MWCNT distributions to investigate the dependence of the electromagnetic response of the composites on the direction of the incident field. Unless otherwise noted, the polarization is parallel to the "L" axis which is the general alignment direction of the MWCNTs.

A. ELECTROMAGNETIC RESPONSE OF THE RECONSTRUCTED 3D MWCNT DISTRIBUTIONS

Four different composites were considered in this work with MWCNT volume fractions equal to [(0.44 ± 0.007) %, (2.58 ± 0.25) %, (4.04 ± 0.19) %, and (6.89 ± 0.43) %] based on the available experimental TEM data. In the successive analysis, these MWCNT volume fractions will be rounded and the composites will be labelled as 0.5 %, 3 %, 4 %, or 7 %, respectively. The dimensions of the unit cell for the 0.5 % volume fraction composite were 800 nm × 800 nm × 200 nm, whereas the dimensions for the other three volume fractions were 200 nm × 200 nm × 200 nm. Smaller dimensions were used for the unit cell of the higher volume fractions to encapsulate a small enough number of MWCNTs that could be simulated in a feasible computational time. Due to the difference in the unit cell size, in the subsequent sections, the results for the 0.5 % MWCNT composite are plotted in different figures than the other volume fractions.

Figure 2 shows a representation of the 0.5 % volume fraction composite where each MWCNT is shown as an arbitrarily-shaped thin wire. On the other hand, top views of the mesh of the 3 %, 4 %, and 7 % MWCNT volume fraction composites are shown in Fig. 6, along with the length distributions of these composites. Similar to Fig. 2c, the unit cells in Fig. 6 had periodic boundary conditions enforced to emulate MWCNT laminates whose lateral dimensions are significantly larger than their thickness.

Figure 7(a) shows the reflection magnitude calculated using CST MWS for the 0.5 % MWCNT composite for both Case A (all walls metallic and large relaxation times) and Case B (only two metallic walls with large relaxation time) conductivities. Both cases have the same relaxation time as shown in Table 2. However, they differ in the number of conducting walls as shown in Fig. 3. Figure 7(a) shows that for Case A, the resonances exhibit a blue shift in comparison to those of Case B. This can be explained by the real(ε_r) of Case A having a larger negative value than that of Case B, as shown in Fig. 4(c), which causes the resonances of a plasmonic nanoparticle to shift to higher frequencies [42]. In other words, based on the length of a MWCNT, it will exhibit a plasmon resonance at a specific negative value of the real(ε_r). If a horizontal line is drawn across Fig. 4c, to indicate a specific real(ε_r) value, we can see that it will intersect Case A curve at a higher frequency than that of the Case B curve. Figure 7(a) shows that the reflection coefficient has a similar magnitude for both Case A and Case B conductivities up to 3 THz. This frequency range is too low for the MWCNTs to resonate for the dimensions studied in this work. Beyond this frequency range, the magnitude of the reflection coefficient of Case B is initially larger than that of Case A since the MWCNTs of Case B resonate at lower frequencies. However, comparing the magnitude of the peaks of both cases shows that Case A yields higher peaks than Case B. This can be explained by Case A having a higher Real(σ_{3D}) than Case B, as shown in Fig. 4(a), which increases the reflection from the composite.

Figure 7(b) compares the reflection magnitude for the same 0.5 % volume fraction composite but in this case, the Case B, Case C, and Case D conductivity models are used for each MWCNT. These three conductivity models have the same number of metallic walls but have progressively larger values for the ζ parameter, which lowers the relaxation time for the walls τ as summarized in Table 2. Beyond 3 THz, where the MWCNTs exhibit resonances, the three conductivities have the same negative value for Real(ε_r), which is the main factor that determines the resonance frequency [42]. Therefore, the three conductivity cases, Case B, Case C, and Case D, exhibit resonances at exactly the same frequencies. Figure 7(b) shows that as the relaxation time decreases, the reflection peaks decrease in amplitude because of the

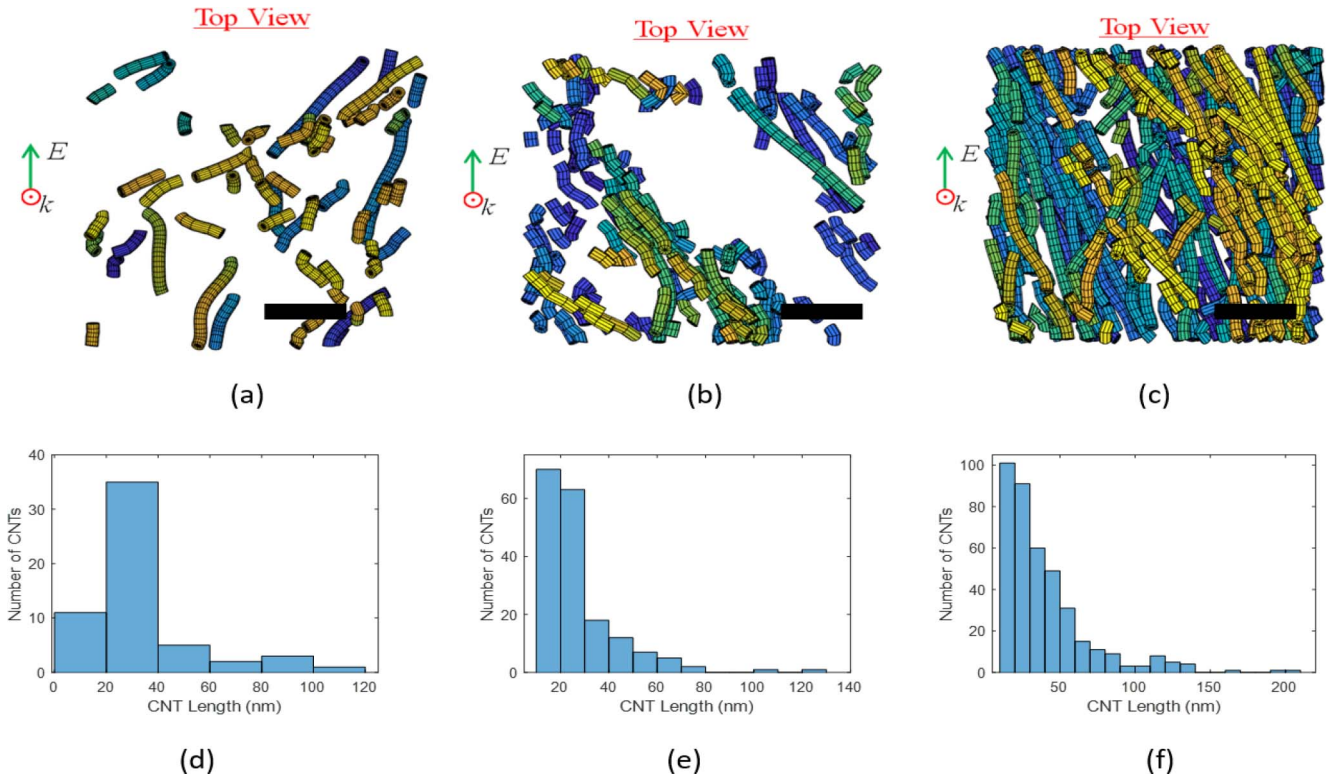

FIGURE 6. Morphological information for the analysis of three volume fraction MWCNT assemblies (a) Top view of the sample of volume fraction = 3 %, (b) volume fraction = 4 % and (c) volume fraction = 7 % along with the imposed electric field, which is vertical as indicated by the green arrow. All scale bars in Fig. 6(a)-(c) represent 50 nm and the color indicate the relative depth of the CNT segment into the page. Fig. 6 (d), (e) and (f) show the MWCNT length distributions in the 3 %, 4 % and 7 % volume fraction composites.

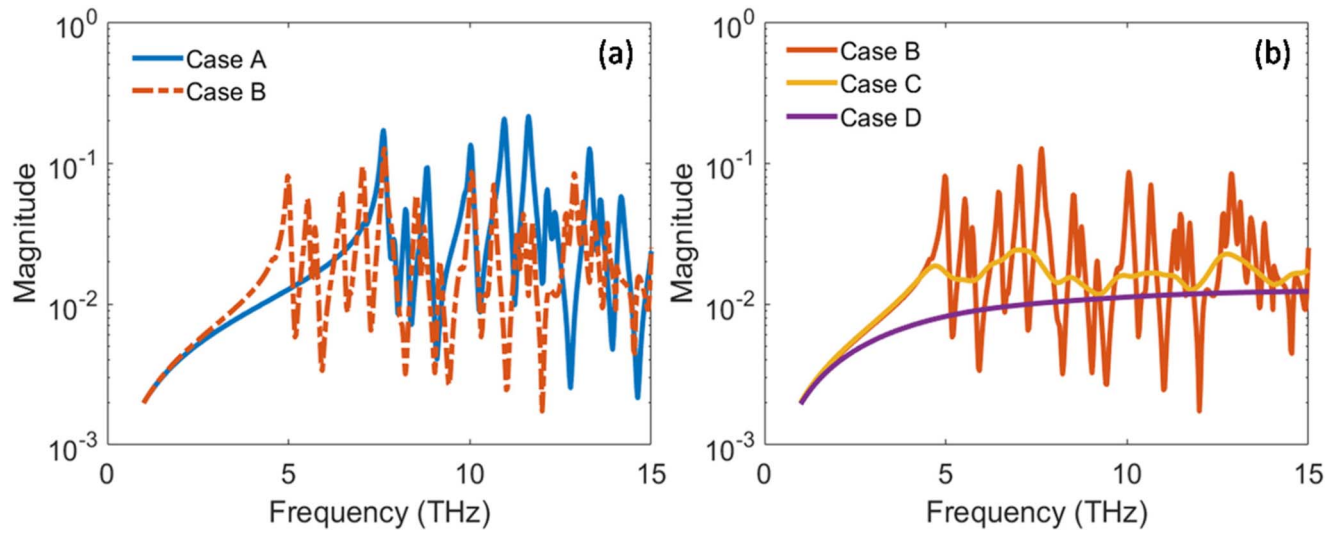

FIGURE 7. Comparison between the magnitude of the reflection coefficient for (a) Case A and Case B conductivities and (b) Case B, Case C, and Case D conductivities for the 0.5 % volume fraction composite. Case A conductivity is where the 5 walls of each MWCNT are metallic with $\zeta = 6$ m/Ks. Case B, C, and D is where only 2 walls of each MWCNT are metallic with $\zeta = 6$ m/Ks, $\zeta = 60$ m/Ks, and $\zeta = 600$ m/Ks, respectively.

decrease in Real(σ_{3D}). This decrease in the Real(σ_{3D}) also causes the quality factor of the resonances to decrease, causing the bandwidth of the resonances to increase and the adjacent resonances to overlap and coalesce. Therefore, Case C shows a few wideband peaks, unlike Case B, which shows numerous sharp isolated resonances. Case D has a significantly lower Real(σ_{3D}) than the other cases, and therefore, the peaks of the resonances are hard to distinguish. Based on our computational experiments, we found that a relaxation time in the femtosecond range or lower, i.e., ζ values in the thousands or larger, causes the resonances to disappear as the MWCNT becomes an over damped system.

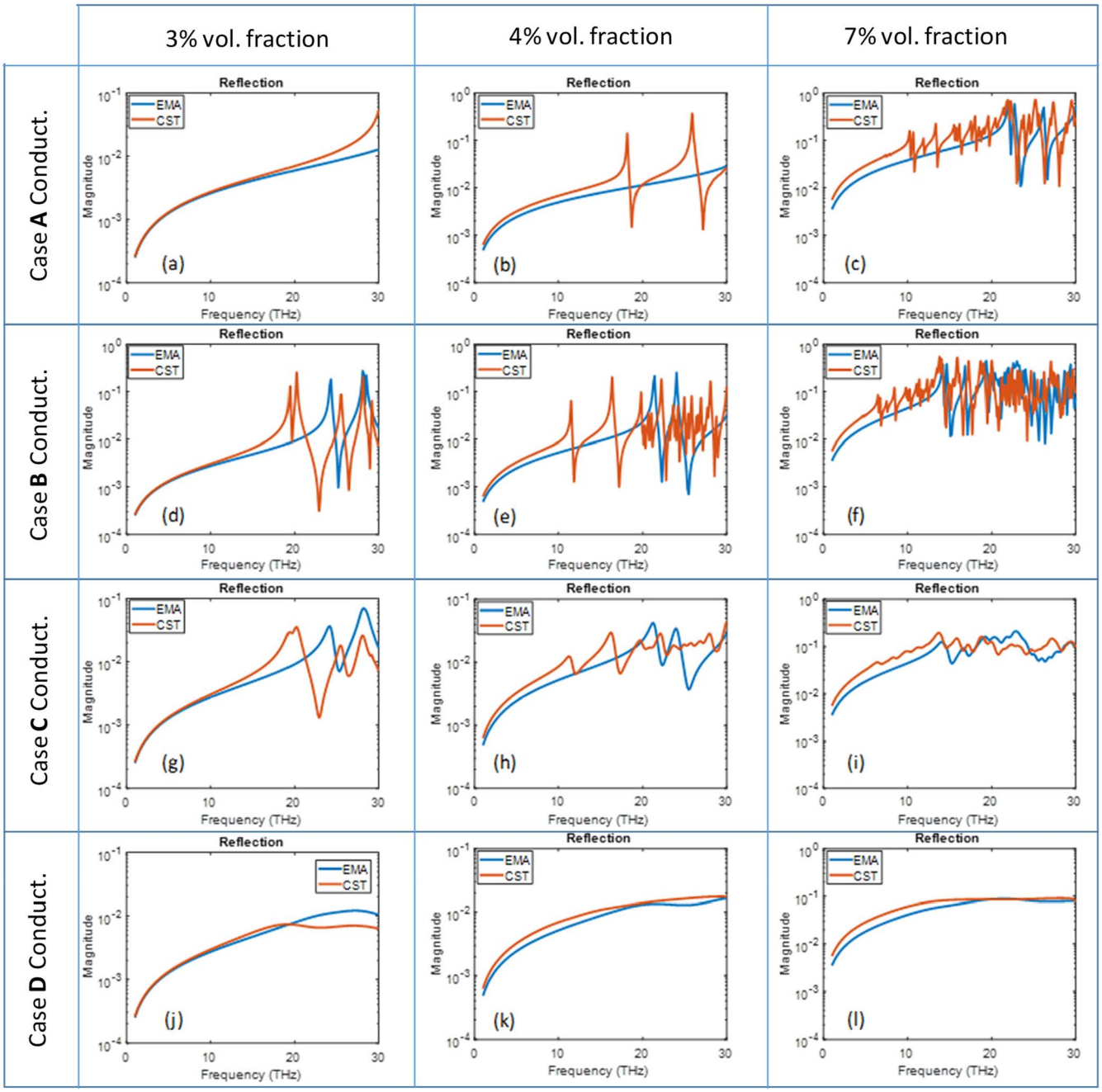

FIGURE 8. Reflection from the MWCNT composite calculated using Full-wave CST simulations and dilute limit effective medium approximations for: (a) volume fraction 3 % and Case A conductivity, (b) volume fraction 4 % and Case A conductivity, (c) volume fraction 7 % and Case A conductivity, (d) volume fraction 3 % and Case B conductivity, (e) volume fraction 4 % and Case B conductivity, (f) volume fraction 7 % and Case B conductivity, (g) volume fraction 3 % and Case C conductivity, (h) volume fraction 4 % and Case C conductivity, (i) volume fraction 7 % and Case C conductivity, (j) volume fraction 3 % and Case D conductivity, (k) volume fraction 4 % and Case D conductivity, (l) volume fraction 7 % and Case D conductivity. Case A conductivity is where the 5 walls of each MWCNT are metallic with $\zeta = 6$ m/Ks. Case B, C, and D is where only 2 walls of each MWCNT are metallic with $\zeta = 6$ m/Ks, $\zeta = 60$ m/Ks, and $\zeta = 600$ m/Ks, respectively.

In summary, Fig. 7 shows that an increase in the magnitude of the negative Real(ε_r) of the MWCNTs causes a composite to exhibit resonances at higher frequencies. Decreasing the Real(σ_{3D}) causes the peak amplitude of the resonances to decrease and the bandwidth of the resonances to increase.

Figure 8 shows the magnitude of the reflection coefficient from the composites with 3 %, 4 %, and 7 % MWCNT volume fractions, calculated using both the full-wave CST MWS simulation and the EMA. In the EMA, the polarizability of the MWCNTs is estimated using the expression for the ellipsoid polarizability in (7). Each column in Fig. 8 corresponds to one of the three-volume fractions considered, whereas each row corresponds to one of the four conductivity cases listed in Table 2 and Fig. 3. Figures 8(a)-(c) show that increasing the MWCNT volume fraction increases the magnitude of the reflection coefficient as expected.

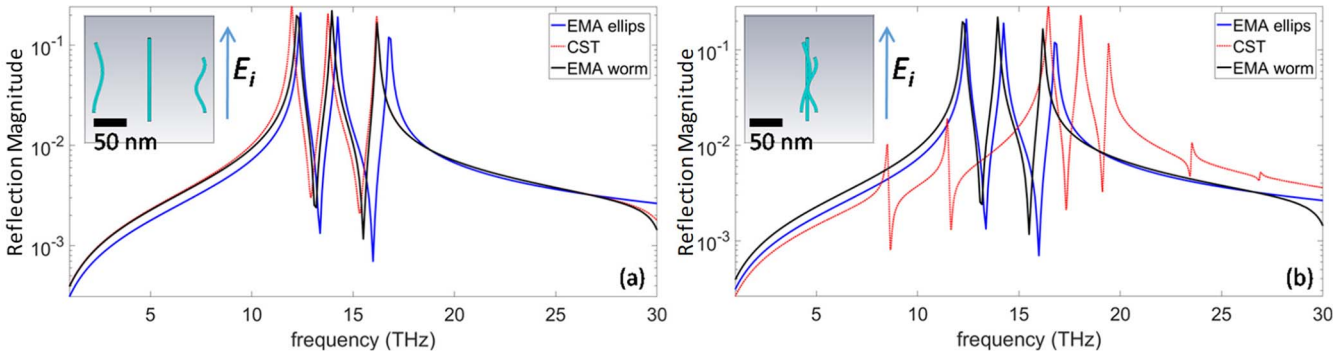

FIGURE 9. Comparison between the magnitude of reflection calculated using: CST MWS, the EMA using the MOM ATW polarizability, and the EMA using the ellipsoid polarizability when (a) the MWCNTs are widely separated and when (b) the same MWCNTs are clustered in close proximity. The lengths of the MWCNTs are 195 nm, 135 nm, and 165 nm. The scale bar represents 50 nm.

Moreover, up to a frequency of 20 THz, good agreement can be seen between the reflection magnitude calculated using CST MWS and that calculated using the EMA for the 3 % volume fraction composite in Fig. 8(a). This agreement starts to deteriorate as the MWCNT volume fraction increases to 4 % and 7 % in Fig. 8(b) and Fig. 8(c), respectively. This can be explained by the fact that the dilute limit EMA is only valid for low MWCNT volume fractions and its predictions starts to diverge from the true effective properties of the composite as the volume fraction of the additive increases and interactions between neighboring MWCNTs becomes more important [43].

In the second row of the figure, Fig. 8(d)-(f), we can see that the resonances shift to lower frequencies, similar to the behavior previously described in Fig. 7. The EMA reflection shown in blue in Fig. 8(f) exhibits additional low-frequency resonances, below 20 THz, which are absent in Fig. 8(d)-8(e). This can be explained by the presence of longer MWCNTs in the 7% composite, $>$ 120 nm, which can be seen by comparing the MWCNT length histogram in Fig. 6(f) with those in Fig. 6(d) and 6(e). A key observation in Fig. 8(d)-(f) is that the full-wave reflection calculated using CST MWS exhibits additional resonances that are absent from the reflection calculated using the EMA. Some of these additional resonances are at lower frequencies and some of them are higher than those exhibited using the EMA. The EMA yields resonances in the reflection magnitude that directly correspond to the MWCNT lengths available in the unit cells in Fig. 6. The additional resonances in the reflection magnitude calculated using CST MWS are due to the strong electromagnetic coupling between the MWCNTs that are in close proximity [13]. Even though the volume fractions studied in this work are relatively low, every unit cell in Fig. 6 clearly show clusters where MWCNTs are in close proximity. These MWCNT clusters lead to the emergence of the additional resonances [13]. That is, if two MWCNTs with identical lengths and slightly different shapes are brought together in close proximity their plasmon resonance will split into two resonances, one at a lower frequency and one at a higher frequency than the resonance of the individual MWCNTs [13]. The 3D tomography reconstructions performed in this work clearly show that the MWCNTs are not uniformly distributed and exhibit clusters that can significantly impact the electromagnetic response of the composites. Comparing the general trend of Fig. 8(f) with Fig. 8(e), we can see that increasing the volume fraction of the MWCNTs increases, on average, the magnitude of the reflection coefficient, as expected.

Similar behavior is exhibited by Case C conductivity as shown in Fig. 8(g)-(i). However, the bandwidths of the resonances increase, causing several resonances to merge leading to an overall broadband response especially for the 7 % volume fraction in Fig. 8(i). For Case D conductivity, which has two metallic walls out of five and the lowest value for the relaxation time, the plasmon resonances in the reflection coefficient disappear due to the small relaxation time for this case and the lower effective MWCNT conductivity. However, for most frequencies in Fig. 8(g)-(i), the full-wave CST MWS reflection shows higher reflection than the EMA counterpart.

In summary, the main conclusion from Fig. 8 is that at low frequencies, well below the plasmon resonance frequencies of the MWCNTs, good agreement can be achieved between the EMA and the full-wave simulation of the composite's electromagnetic response. At higher frequencies, this agreement deteriorates, especially for high MWCNT volume fractions or for higher MWCNT conductivities. The breakdown in agreement is caused by the strong electromagnetic interaction between the MWCNTs as will be illustrated in the following sub-section.

B. ELECTROMAGNETIC RESPONSE OF SIMPLE MWCNT DISTRIBUTIONS

To confirm the findings of the previous subsection, the simple composite shown in Fig. 9 is simulated. The unit cell of the composite shown in Fig. 9 contains only three MWCNTs that are 195 nm, 135 nm, and 165 nm in length and have an outer radius of 3.86 nm. Two composites are studied in Fig. 9. In Figure 9(a), the MWCNTs are widely separated whereas in Fig. 9(b) the MWCNTs are concentrated in a tight cluster. In both cases, the MWCNTs are in different planes in the perpendicular direction and they do not intersect and they are embedded in a 200 nm $\times$ 200 nm $\times$

200 nm unit cell. The same conductivity, Case B, is assigned to the MWCNTs in each case. In Case B, two walls out of the five walls of each MWCNT are metallic but they have the largest relaxation time. In Figure 9, the top view of the composite is shown in a way similar to the images typically achieved using SEM. From a single view, it is hard to identify if the MWCNTs are widely separated in the perpendicular direction or if they are closely clustered. Hence, 3D tomography provides significantly more information about the MWCNT distribution, which determines the electromagnetic response. The polarization is parallel to the "L" axis which is the general alignment direction of the MWCNTs as shown in Fig. 9.

For the EMA calculations, we used two different approaches for calculating the polarizability of each MWCNT: the MOM for ATW formulation in (6) and the ellipsoid polarizability in (7). In Figure 9(a), the reflection calculated using the EMA shows three distinct resonances that correspond to the three different MWCNT lengths. In Figure 9(a), the MWCNTs are widely separated and therefore they exhibit insignificant electromagnetic coupling. Therefore, the full-wave reflection calculated using CST MWS also exhibits only three resonances. Since the MWCNTs are not straight, using the MOM for ATW to calculate the MWCNT polarizability yields better agreement with the full-wave CST MWS reflections than the ellipsoid polarizability in the EMA approach. However, the difference between the two polarizability estimates is not significant, indicating that this is not the main reason for the major difference between the full-wave response and the EMA in Fig. 8.

Figure 9(b) shows the same MWCNTs in the same unit cell, with the same volume fraction as the composite in Fig. 9a. However, the MWCNTs in Fig. 9(b) are grouped into a tighter cluster and therefore they exhibit much stronger electromagnetic coupling. This causes the reflection calculated using the full-wave CST MWS to exhibit seven resonances even though only three MWCNTs of different lengths are considered. The additional resonances emerge due to the splitting of the individual resonances of the three MWCNTs. This splitting occurs when the MWCNTs have slight differences in shape and are grouped together in a tight bundle as discussed in [13]. The reflection calculated using the EMA combined with the ellipsoid polarizability or with the MOM for ATW polarizability show significant differences with the full-wave reflection. The comparison between Fig. 9(b) and Fig. 9(a) clearly shows that the clustering of MWCNTs, even for low volume fractions, can lead to strong electromagnetic interaction and resonance splitting, which agrees with the results shown in Fig. 8 for the reconstructed MWCNT composites. As the number of MWCNTs increases, the number of clusters also increases, and many additional modes emerge that can overlap and lead to an overall broadband electromagnetic response.

The results in Fig. 8 and Fig. 9 show the importance of accounting for the strong electromagnetic coupling between MWCNTs when interpreting the measured reflection or any other electromagnetic response of an MWCNT composite. For example, if the MWCNT electromagnetic interactions are neglected and the response in Fig. 9(b) is interpreted using only the EMA, false conclusions might be obtained that seven different MWCNT lengths are present in the composite and none of them match with the three MWCNT lengths actually present in the composite. However, if the volume fraction and the length distribution of the MWCNTs in the composite are known beforehand, the electromagnetic response can provide information about the clustering of the MWCNTs. That is, if the resonances in the electromagnetic response correspond directly to the length distributions with no additional resonances, this indicates that the MWCNTs are widely separated. If however, additional resonances are apparent in the electromagnetic response or if the bandwidth of the electromagnetic response is significantly broader than the range of the length distributions, this indicates that some of the MWCNTs are arranged in tight bundles or clusters.

The MWCNTs in the fabricated samples were longer than any of the lengths in the length distributions in Fig. 6. However, due to the limitations in 3D electron tomography, only small sections of the composite can be reconstructed. To validate that the conclusions in the previous subsections are also applicable for longer MWCNTs, composites consisting of three longer MWCNTs were simulated in Fig. 10 and Fig. 11. The lengths of the three MWCNTs studied in Fig. 10 were set to 1.4 μm, 1.1 μm, and 1.3 μm, respectively, whereas the lengths of the three MWCNTs studied in Fig. 11 were set to 0.014 mm, 0.011 mm, and 0.013 mm, respectively. In Figure 10, the three MWCNTs were embedded in an identical unit cell that had the dimensions of 1.6 μm x 1.6 μm x 0.200 μm and in Fig. 11 the three MWCNTs were embedded in an identical unit cell that had the dimensions of 0.016 mm x 0.016 mm x 0.002 mm. All the MWCNTs in Fig. 10 and Fig. 11 had identical Case B conductivity and identical radius of 3.86 nm. The polarization is parallel to the "L" axis which is the general alignment direction of the MWCNTs as shown in Fig. 10 and Fig. 11.

In Figure 10, the three tubes were arranged in two different configurations: widely spaced and tightly clustered, as shown in Fig. 10. Therefore, both configurations had identical volume fractions of $\sim 0.035\%$. Since the MWCNTs in the fabricated samples in Fig. 6 were not perfectly straight, the three MWCNTs in Fig. 10 were also set to be non-straight. In the dilute limit EMA, the polarizability of each of the three MWCNTs was calculated using the MOM for ATW formulation in (6) to account for their exact shape. Figure 10(a) shows that, for the case of the widely separated MWCNTs, excellent agreement is achieved between the full-wave and the dilute limit EMA. Compared to Fig. 9, the longer MWCNTs in Fig. 10 cause the resonances in the reflection to shift to lower frequencies. For example, the first resonance in the reflection in Fig. 9(a) occurs around 12 THz, whereas the first resonance in Fig. 10(a) occurs around 2 THz. This shift is in agreement with the ratio between the

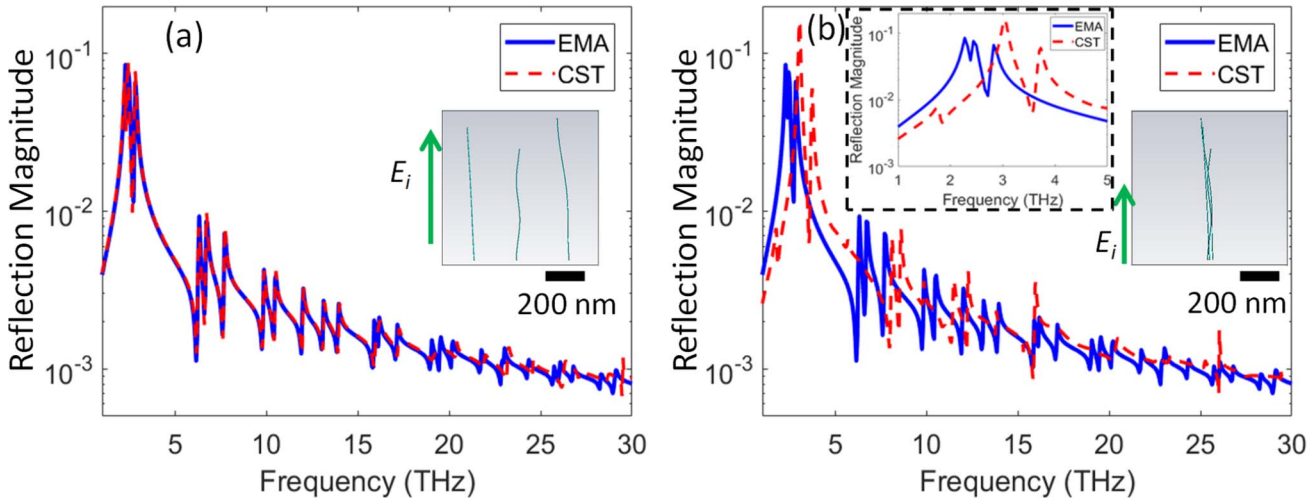

FIGURE 10. Comparison between the reflection magnitude calculated using CST MWS and the EMA using the MOM ATW polarizability when (a) three long MWCNTs are widely separated and when (b) the same MWCNTs are clustered in close proximity. The lengths of the MWCNTs are 1.4 μm, 1.1 μm, and 1.3 μm. The inset zooms on the reflection magnitude in the 1 THz - 5 THz frequency range. The scale bar represents 200 nm.

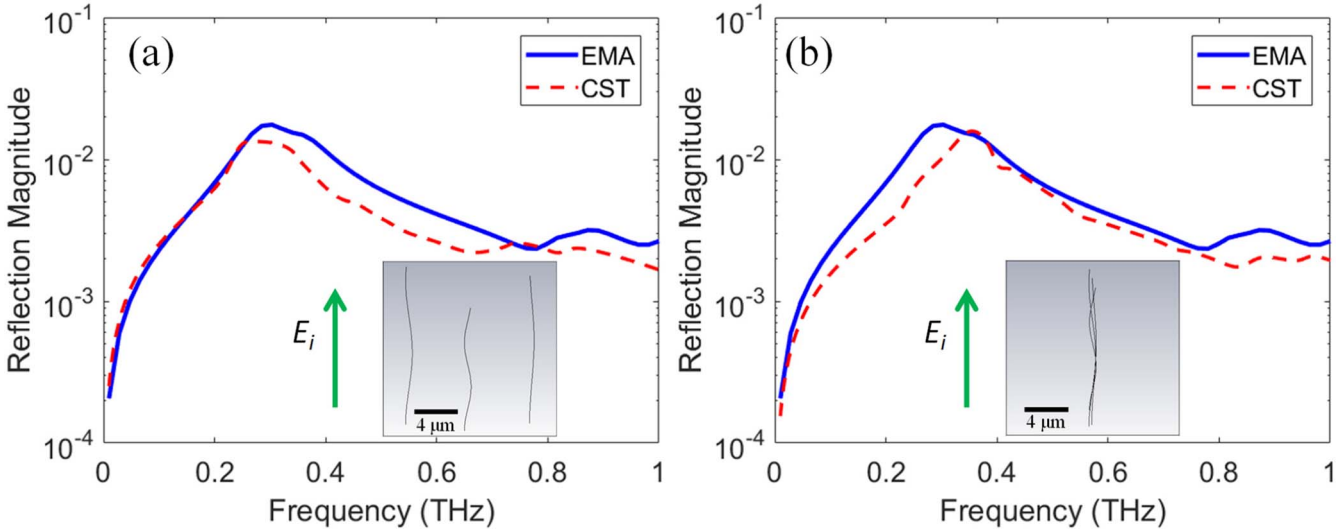

FIGURE 11. Comparison between the reflection magnitude calculated using CST MWS and the EMA using the MOM ATW polarizability when (a) three long MWCNTs are widely separated and when (b) the same MWCNTs are clustered in close proximity. The lengths of the MWCNTs are 0.014 mm, 0.011 mm, and 0.013 mm. The scale bar represents 4 μm.

lengths of the MWCNTs in Fig. 9(a) and those in Fig. 10(a). The reflection in Fig. 10(a) had significantly more resonances than those in Fig. 9(a) even though both cases only had three MWCNTs per unit cell. This can be explained by the longer MWCNTs in Fig. 10(a) exhibiting higher-order resonances in the 1 THz – 30 THz frequency range [12], [13]. The same higher-order resonances will occur for the composites in Fig. 9(a) if frequencies higher than 30 THz are considered.

When the same MWCNTs were clustered in close proximity, the reflection calculated using the full-wave CST MWS solver differed significantly from the dilute limit EMA as shown in Fig. 10(b). Again this can be attributed to the interactions between the MWCNTs in close proximity. The results in Fig. 10(b) show that the inaccuracy of the dilute limit EMA in calculating the electromagnetic response of MWCNTs clustered in close proximity. Typically, MWCNTs and other nanoparticles exhibit strong electromagnetic coupling when they are separated by less than 4-5 times their radius as shown in Fig. 9(b) and Fig. 10(b) [44], [45].

Figure 11 shows longer MWCNTs also in a widely separated and in a close proximity formations. These longer MWCNTs resonate at a lower frequency range and therefore in order to reduce the computational time we limited the frequency range of the simulation to range from 0.10 THz to 1 THz. Similar to Fig. 10, Fig. 11a shows good agreement, in the 0.01 THz to 0.25 THz frequency range, between the reflection magnitude calculated using the dilute limit EMA and the reflection magnitude calculated using CST MWS for the case of widely separated MWCNTs. The agreement worsens for the case of the MWCNTs in close proximity, shown in Fig 11b, due to also the strong electromagnetic interactions between the MWCNTs. In Fig. 11b, we believe

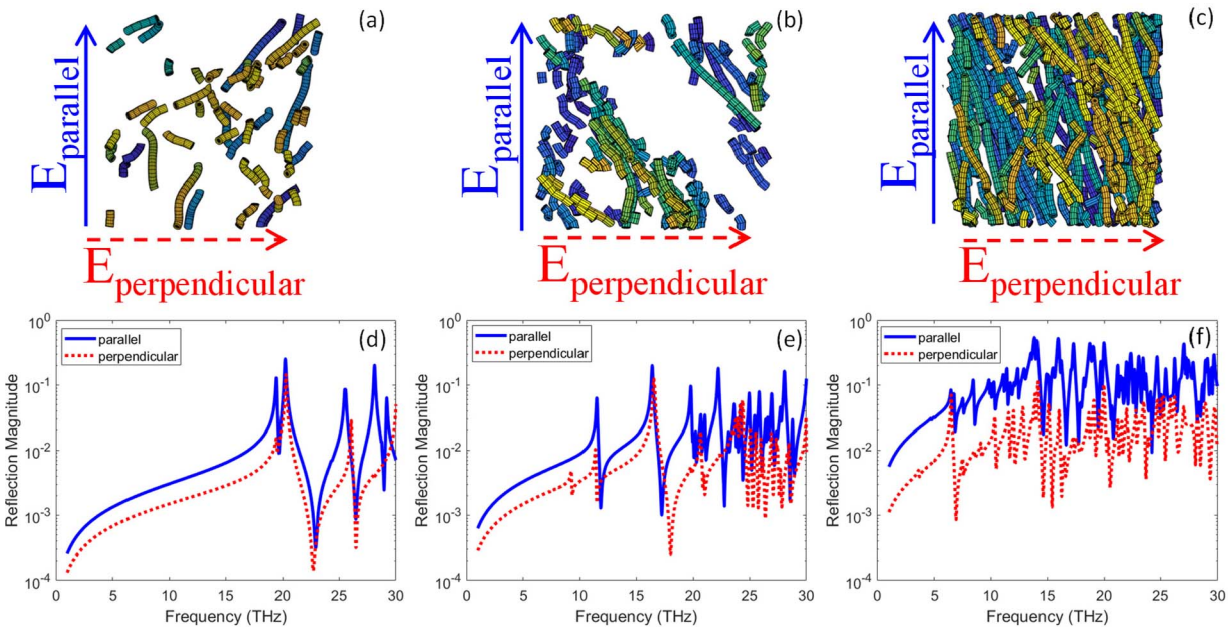

FIGURE 12. Comparison between the reflection magnitude for different incident electric field directions. The top view of the (a) 3% unit cell, (b) 4%, (c) 7% and the two electric field directions tested are illustrated. The corresponding reflection magnitude for the (d) 3 %, (e) 4 %, and (f) 7 % MWCNT volume fraction.

that the agreement between CST and the EMA across the frequency range 0.3 THz to 0.8 THz is merely coincidental based on the results in the previous figures.

The variation in the full-wave response of a composite with the MWCNT distribution shown in Fig. 10 and Fig, 11 shows the strength of electromagnetic waves in probing different distributions of MWCNTs, which has significant potential for the NDE of composites. Future work will include developing a clustering parameter that provides information about the MWCNTs clusters (e.g., the number of tubes/cluster, the size of the cluster) and studying how to extract this parameter from the electromagnetic response of the composite.

C. ANISOTROPY OF ELECTROMAGNETIC RESPONSE

One of the motivations behind fabricating aligned and straight MWCNT composites is to develop anisotropic materials that vary their response based on the direction of the incident field. For example, several studies have reported terahertz polarizers composed of highly aligned SWCNTs and MWCNTs [46], [47]. In this work, the availability for the first time of the exact 3D distribution of MWCNTs allows us to quantify the anisotropy in the electromagnetic response at different MWCNT densities. Fig. 12 shows the reflection magnitude of the 3%, 4%, and 7% composites when the polarization is parallel and perpendicular to the "*L*" axis. Fig. 12a, Fig. 12b, and Fig. 12c show the direction of the parallel and the perpendicular polarization with respect to the reconstructed 3D MWCNT distribution for the 3%, 4%, and 7% composites, respectively. In Fig. 12d to Fig. 12f, the solid blue curve is the simulated reflection when the incident polarization is parallel to "*L*" and the dashed red curve is simulated reflection when the incident polarization is perpendicular to "*L*". Both polarizations were calculated using the full-wave CST MWS solver and Case B (only two metallic walls with large relaxation time) conductivity for the MWCNTs. The three subplots in Fig. 12(a)-12(c) show that higher reflection is achieved when the incident electric field is parallel to the general alignment of the MWCNTs, "*L*", which is expected [46], [47]. This is clear at very low frequencies before the onset of the plasmon resonances. By comparing Fig. 12(a)–12(c), it seems that the gap between the reflections of both directions widens as the MWCNT volume density increases. To clarify this trend, we calculated, at each frequency in Fig. 12, the anisotropy ratio by dividing the reflection when the incident polarization is parallel to "*L*" with the reflection when the incident polarization is perpendicular to "*L*". The average of this anisotropy ratio over the frequency range spanning 1 THz to 30 THz was then calculated for each of the three volume fractions in Fig. 12. Fig. 13 shows this average anisotropy ratio versus the MWCNT volume fraction and it shows that the anisotropy in the electromagnetic response increases with the MWCNT volume fraction. This increase is in agreement with reported experimental measurements, which show that MWCNTs become straighter and more aligned as their density inside the composite increases and hence their anisotropy ratio increases [23]. Therefore, by probing composites at multiple incident field directions, the straightness and alignment of the MWCNTs can be evaluated.

In summary, this paper shows that accurate 3D reconstruction of MWCNT distributions can be used to quantify the full-wave electromagnetic response of composites with different densities and with different levels of alignment.

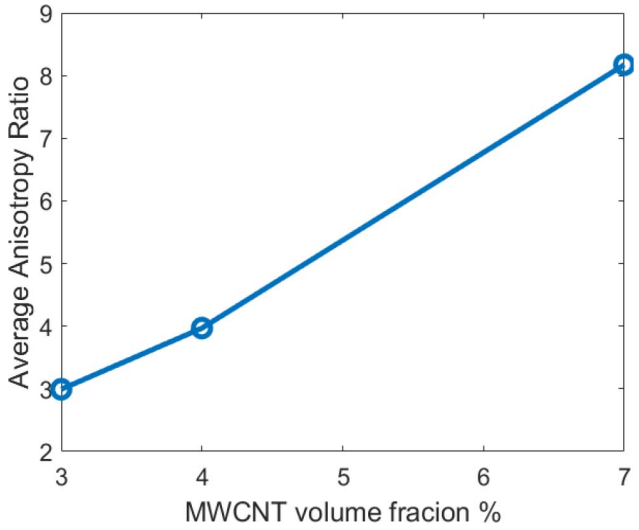

FIGURE 13. Calculated average reflection anisotropy ratio for composites with different MWCNT volume fractions.

Once this behavior is quantified, calibration curves like those presented in Fig. 13 can be generated for use in future electromagnetic NDE of composites. For example, the average reflection anisotropy ratio can be measured experimentally on a composite and then, using Fig. 13, the level of alignment and possibly the volume fraction of the MWCNTs in the composite could be retrieved. Future work will involve conducting experimental measurements to validate the accuracy of these NDE approaches.

V. CONCLUSION AND FUTURE WORK

In this work, the experimental reconstruction of several multi-walled carbon nanotube (MWCNT) three-dimensional (3D) distributions using electron tomography provided vital information about the shapes and locations of the MWCNTs inside the composite. This information was used, for the first time, in the simulation of the electromagnetic response of MWCNT composites using full-wave simulations and the dilute limit effective medium approximation (EMA). The results show that the electromagnetic response calculated using the dilute limit EMA differs significantly from the full-wave simulations, especially at higher THz frequencies, due to strong interactions between adjacent MWCNTs, even at small volume fractions. Both the full-wave simulations and EMAs confirm that the magnitude of reflection increases with the increase in the volume fraction. However, the differences between the full-wave simulations and the EMAs increase with increasing volume fraction as expected. The MWCNTs resonate at higher frequencies when the real part of their effective relative dielectric permittivity is more negative. The sharpness of these resonances is dependent on the relaxation time, where the resonant peaks become narrower as the relaxation time increases. It was shown that by using multiple incident field directions that the anisotropy in the electromagnetic response of the MWCNT composites can be accurately quantified. This anisotropy can be then used to evaluate the straightness and alignment of the MWCNTs in the composite material.

Overall, the results of this paper show that these experimentally characterized 3D MWCNT maps act as useful testbeds for understanding the electromagnetic response of nanocomposites. Our future work will extend this characterization to a mixture of different conductivity MWCNTs and the use of a material different from air as the embedding medium. In addition, guidelines will be developed to help correlate the electromagnetic response of a composite with the actual MWCNT distribution and properties, the reverse problem of what was done here.

REFERENCES

[1] M. González, J. Pozuelo, and J. Baselga, "Electromagnetic shielding materials in GHz range," *Chem. Rec.*, vol. 18, nos. 7–8, pp. 1000–1009, Jul. 2018.

[2] M. Martin-Gallego, V. Yuste-Sanchez, R. Sanchez-Hidalgo, R. Verdejo, and M. A. Lopez-Manchado, "Epoxy nanocomposites filled with Carbon nanoparticles," *Chem. Rec.*, vol. 18, nos. 7–8, pp. 928–939, Jul. 2018.

[3] D. Kim, S.-E. Lee, K. Chu, S.-H. Park, and Y. Sohn, "Carbon nanotube nanocomposite having segregated network structure for wearable thermotherapy application," *IEEE Electron Device Lett.*, vol. 38, no. 10, pp. 1489–1491, Oct. 2017.

[4] A. M. Marconnet, N. Yamamoto, M. A. Panzer, B. L. Wardle, and K. E. Goodson, "Thermal conduction in aligned Carbon nanotube–polymer nanocomposites with high packing density," *ACS Nano*, vol. 5, no. 6, pp. 4818–4825, Jun. 2011.

[5] B. Gorain *et al.*, "Carbon nanotube scaffolds as emerging nanoplatform for myocardial tissue regeneration: A review of recent developments and therapeutic implications," *Biomed. Pharmacother*, vol. 104, pp. 496–508, Aug. 2018.

[6] C. Liu, I. Sergeichev, I. Akhatov, and K. Lafdi, "CNT and polyaniline based sensors for the detection of acid penetration in polymer composite," *Compos. Sci. Technol.*, vol. 159, pp. 111–118, May 2018.

[7] B. N. Bhat, *Aerospace Materials and Applications*. Reston, VA, USA: Amer. Inst. Aeronautics Astronautics, 2018.

[8] M. F. De Volder, S. H. Tawfick, R. H. Baughman, and A. J. Hart, "Carbon Nanotubes: Present and future commercial applications," *Science*, vol. 339, no. 6119, pp. 535–539, 2013.

[9] R. Beigmoradi, A. Samimi, and D. Mohebbi-Kalhori, "Engineering of oriented Carbon Nanotubes in composite materials," *Beilstein J. Nanotechnol.*, vol. 9, pp. 415–435, Feb. 2018.

[10] N. D. Orloff *et al.*, "Dielectric characterization by microwave cavity perturbation corrected for nonuniform fields," *IEEE Trans. Microw. Theory Techn.*, vol. 62, no. 9, pp. 2149–2159, Sep. 2014.

[11] A. M. Hassan, J. Obrzut, and E. J. Garboczi, "A Q-band free-space characterization of Carbon nanotube composites," *IEEE Trans. Microw. Theory Techn.*, vol. 64, no. 11, pp. 3807–3819, Nov. 2016.

[12] A. M. Hassan, F. Vargas-Lara, J. F. Douglas, and E. J. Garboczi, "Electromagnetic resonances of individual single-walled Carbon Nanotubes with realistic shapes: A characteristic modes approach," *IEEE Trans. Antennas Propag.*, vol. 64, no. 7, pp. 2743–2757, Jul. 2016.

[13] A. M. Hassan, F. Vargas-Lara, J. F. Douglas, and E. J. Garboczi, "Electromagnetic scattering from multiple single-walled Carbon Nanotubes having tumbleweed configurations," *IEEE Trans. Antennas Propag.*, vol. 65, no. 6, pp. 3192–3202, Jun. 2017.

[14] A. M. Hassan and E. J. Garboczi, "Electromagnetic scattering from randomly-centered parallel single-walled Carbon Nanotubes embedded in a dielectric slab," *IEEE Trans. Antennas Propag.*, vol. 62, no. 10, pp. 5230–5241, Oct. 2014.

[15] F. Vargas-Lara, A. M. Hassan, E. J. Garboczi, and J. F. Douglas, "Intrinsic conductivity of Carbon Nanotubes and graphene sheets having a realistic geometry," *J. Chem. Phys.*, vol. 143, no. 20, Nov. 2015, Art. no. 204902.

[16] B. Natarajan *et al.*, "Multiscale metrologies for process optimization of Carbon nanotube polymer composites," *Carbon*, vol. 108, pp. 381–393, Nov. 2016.

[17] A. Lakhtakia, G. Y. Slepyan, S. A. Maksimenko, A. V. Gusakov, and O. M. Yevtushenko, "Effective medium theory of the microwave and the infrared properties of composites with Carbon nanotube inclusions," *Carbon*, vol. 36, no. 12, pp. 1833–1839, 1998.

[18] G. Y. Slepyan, M. V. Shuba, S. A. Maksimenko, C. Thomsen, and A. Lakhtakia, "Terahertz conductivity peak in composite materials containing Carbon Nanotubes: Theory and interpretation of experiment," *Phys. Rev. B, Condens. Matter*, vol. 81, no. 20, May 2010, Art. no. 205423.

[19] M. V. Shuba *et al.*, "Experimental evidence of localized plasmon resonance in composite materials containing single-wall Carbon Nanotubes," *Phys. Rev. B, Condens. Matter*, vol. 85, no. 16, Apr. 2012, Art. no. 165435.

[20] M. V. Shuba, A. V. Melnikov, A. G. Paddubskaya, P. P. Kuzhir, S. A. Maksimenko, and C. Thomsen, "Role of finite-size effects in the microwave and subterahertz electromagnetic response of a multiwall Carbon-nanotube-based composite: Theory and interpretation of experiments," *Phys. Rev. B, Condens. Matter*, vol. 88, no. 4, Jul. 2013, Art. no. 045436.

[21] E. Dadrasnia, S. Puthukodan, and H. Lamela, "Terahertz electrical conductivity and optical characterization of composite nonaligned single-and multiwalled Carbon Nanotubes," *J. Nanophoton.*, vol. 8, no. 1, 2014, Art. no. 083099.

[22] F. Fisher, "Fiber waviness in nanotube-reinforced polymer composites—I: Modulus predictions using effective nanotube properties," *Compos. Sci. Technol.*, vol. 63, no. 11, pp. 1689–1703, Aug. 2003.

[23] B. Natarajan *et al.*, "The evolution of Carbon nanotube network structure in unidirectional nanocomposites resolved by quantitative electron tomography," *ACS Nano*, vol. 9, no. 6, pp. 6050–6058, Jun. 2015.

[24] B. L. Wardle, D. S. Saito, E. J. García, A. J. Hart, R. G. de Villoria, and E. A. Verploegen, "Fabrication and characterization of ultrahigh-volume- fraction aligned Carbon nanotube-polymer composites," *Adv. Mater.*, vol. 20, no. 14, pp. 2707–2714, Jul. 2008.

[25] H. Cebeci, R. G. de Villoria, A. J. Hart, and B. L. Wardle, "Multifunctional properties of high volume fraction aligned Carbon nanotube polymer composites with controlled morphology," *Compos. Sci. Technol.*, vol. 69, nos. 15–16, pp. 2649–2656, Dec. 2009.

[26] I. Y. Stein, D. J. Lewis, and B. L. Wardle, "Aligned Carbon nanotube array stiffness from stochastic three-dimensional morphology," *Nanoscale*, vol. 7, no. 46, pp. 19426–19431, 2015.

[27] I. Y. Stein and B. L. Wardle, "Mechanics of aligned Carbon nanotube polymer matrix nanocomposites simulated via stochastic three-dimensional morphology," *Nanotechnology*, vol. 27, no. 3, Jan. 2016, Art. no. 035701.

[28] S. A. Hashemi, S. M. Mousavi, M. Arjmand, N. Yan, and U. Sundararaj, "Electrified single-walled Carbon nanotube/epoxy nanocomposite via vacuum shock technique: Effect of alignment on electrical conductivity and electromagnetic interference shielding," *Polym. Compos.*, vol. 39, no. S2, pp. E1139–E1148, May 2018.

[29] H. Cebeci, I. Y. Stein, and B. L. Wardle, "Effect of nanofiber proximity on the mechanical behavior of high volume fraction aligned Carbon nanotube arrays," *Appl. Phys. Lett.*, vol. 104, no. 2, Jan. 2014, Art. no. 023117.

[30] J. Lee *et al.*, "Impact of Carbon nanotube length on electron transport in aligned Carbon nanotube networks," *Appl. Phys. Lett.*, vol. 106, no. 5, Feb. 2015, Art. no. 053110.

[31] J. A. Berres and G. W. Hanson, "Multiwall Carbon Nanotubes at RF-THz frequencies: Scattering, shielding, effective conductivity, and power dissipation," *IEEE Trans. Antennas Propag.*, vol. 59, no. 8, pp. 3098–3103, Aug. 2011.

[32] M. V. Shuba, G. Y. Slepyan, S. A. Maksimenko, C. Thomsen, and A. Lakhtakia, "Theory of multiwall Carbon Nanotubes as waveguides and antennas in the infrared and the visible regimes," *Phys. Rev. B, Condens. Matter*, vol. 79, no. 15, Apr. 2009, Art. no. 155403.

[33] B. Liu, F. Wu, H. Gui, M. Zheng, and C. Zhou, "Chirality-controlled synthesis and applications of single-wall Carbon Nanotubes," *ACS Nano*, vol. 11, no. 1, pp. 31–53, Jan. 2017.

[34] H.-S. P. Wong and D. Akinwande, *Carbon Nanotube Graphene Device Physics*. New York, NY, USA: Cambridge Univ. Press, 2011.

[35] G. Y. Slepyan, S. A. Maksimenko, A. Lakhtakia, O. Yevtushenko, and A. V. Gusakov, "Electrodynamics of Carbon Nanotubes: Dynamic conductivity, impedance boundary conditions, and surface wave propagation," *Phys. Rev. B, Condens. Matter*, vol. 60, no. 24, pp. 17136–17149, Dec. 1999.

[36] A. M. Nemilentsau, "Tutorial: Linear surface conductivity of an Achiral single-wall Carbon nanotube," *J. Nanophoton.*, vol. 5, no. 1, Jan. 2011, Art. no. 050401.

[37] G. W. Hanson, "Radiation efficiency of nano-radius dipole antennas in the microwave and far-infrared regimes," *IEEE Antennas Propag. Mag.*, vol. 50, no. 3, pp. 66–77, Jun. 2008.

[38] A. R. AlAjmi and S. F. Mahmoud, "Investigation of multiwall Carbon Nanotubes as antennas in the subterahertz range," *IEEE Trans. Nanotechnol.*, vol. 13, no. 2, pp. 268–273, Mar. 2014.

[39] *Electromagnetic Simulation Software |Altair FEKO*. Accessed: Nov. 12, 2018. [Online]. Available: https://altairhyperworks.com/product/FEKO

[40] *CST MICROWAVE STUDIO 3D EM Simulation Software*. Accessed: Nov. 12, 2018. [Online]. Available: https://www.cst.com/products/cstmws

[41] G. W. Hanson, "Fundamental transmitting properties of Carbon nanotube antennas," *IEEE Trans. Antennas Propag.*, vol. 53, no. 11, pp. 3426–3435, Nov. 2005.

[42] S. A. Maier, *Plasmonics: Fundamentals and Applications*. New York, NY, USA: Springer, 2007.

[43] S. Torquato, *Random Heterogeneous Materials: Microstructure and Macroscopic Properties*. New York, NY, USA: Springer, 2002.

[44] A. M. Hassan *et al.*, "Electromagnetic scattering from multiple Carbon Nanotubes with experimentally determined shapes and distributions," in *Proc. USNC-URSI Radio Sci. Meeting (Joint With AP-S Symp.)*, Vancouver, BC, Canada, 2015, p. 28.

[45] P. K. Jain, W. Huang, and M. A. El-Sayed, "On the universal scaling behavior of the distance decay of plasmon coupling in metal nanoparticle pairs: A plasmon ruler equation," *Nano Lett.*, vol. 7, no. 7, pp. 2080–2088, Jul. 2007.

[46] L. Ren *et al.*, "Carbon Nanotube Terahertz polarizer," *Nano Lett.*, vol. 9, no. 7, pp. 2610–2613, Jul. 2009.

[47] J. Kyoung *et al.*, "A reel-wound Carbon Nanotube polarizer for Terahertz frequencies," *Nano Lett.*, vol. 11, no. 10, pp. 4227–4231, Oct. 2011.